Lappeenranta-Lahti University of Technology LUT
School of Engineering Science
Computational Engineering and Technical Physics
Computer Vision and Pattern Recognition

Nima Bahmani

VITAL SIGN DETECTION USING SHORT-RANGE MM-WAVE PULSED WAVE RADAR

Master's Thesis

Examiners: Associate Professor , Dr. Arto Kaarna
MPhil. Markku Rouvala

Supervisors: Associate Professor , Dr. Arto Kaarna
MPhil. Markku Rouvala

ABSTRACT

Lappeenranta-Lahti University of Technology LUT
School of Engineering Science
Computational Engineering and Technical Physics
Computer Vision and Pattern Recognition

Nima Bahmani

Vital Sign Detection Using Short-Range Mm-Wave Pulsed wave RADAR

Master's Thesis

2020

45 pages, 15 figures, 3 table, 1 appendices.

Examiners: Associate Professor , Dr. Arto Kaarna
MPhil. Markku Rouvala

Keywords: mm-wave RADAR, pulsed wave RADAR, vital sign, signal processing

Proximity sensors have been improving fast during the last decades. Using a radiation source and examining the reflected signal, it is possible to investigate the surrounding environment without contact. The mm-wave RADAR systems demonstrate tremendous potential compared to the other proximity sensing options, which are based on sound or light waves. In this study, a 60 GHz RADAR system was used for vital sign detection, such as respiration and heartbeat rate. The potential of the system in measuring through the materials was investigated in different transmission scenarios. Three different algorithms were tested for extracting the phase information, and a standard heartbeat rate measurement device compared the accuracy of the results. The proposed algorithm can scan the area in the RADAR field of view and obtain remarkable features like the heartbeat rate with a median accuracy of 96.22%.

PREFACE

I would like to express my sincere gratitude to my university supervisor, Arto Kaarna, to guide me through my master's degree. Special thanks to Markku Rouvala, not only for all the support he has shown me in this research but also, leading me towards the right path in life. Further thanks to Huawei company for funding this thesis, and my colleague, Pasi Pylvas, for his generosity and helps. Finally, thanks to my family for their unconditional supports.

Helsinki, November 2, 2020

Nima Bahmani

CONTENTS

LIST OF ABBREVIATIONS

CW	Continuous Wave
DSP	Digital Signal Processing
EEMD	Ensemble Empirical Mode Decomposition
EMD	Empirical Mode Decomposition
FFT	Fast Fourier Transform
GUI	Graphical User Interface
HCI	Human Computer Interaction
I-Q	In-phase-Quadrature
LIDAR	Laser Imaging Detection And Ranging
LPF	Low Pass Filter
MAF	Moving Average Filter
MIMO	Multiple Input Multiple Output
PW	Pulsed Wave
PRF	Pulse Repetition Frequency
PRI	Pulse Repetition Interval
PW	Pulsed Wave
RADAR	Radio Detection And Ranging
RCS	RADAR Cross-Section
SONAR	Sound Navigation And Ranging
TOF	Time Of Flight
UWB	Ultra Wide-Band
WT	Wavelet Transform

LIST OF SYMBOLS

Normal symbols

A	envelope of the transmitted signal
A'	envelope of the received signal
a	lower limit of the range
b	upper limit of the range
c	speed of light
d	range index
d_{peak}	range index with the highest amplitude within a sweep
f_0	frequency
G_r	gain of the received antenna
G_t	gain of the transmit antenna
I	real part of y_{IQ}
L	number of range samples
M	number of sweeps
N	number of samples
P_r	received power
P_t	transmitted power
Q	imaginary part of y_{IQ}
R_0	range from the RADAR to the target
s	sweep index
st	step length
t	time
T_s	sampling interval
ΔT	time of flight
x	RADAR transmitted signal
y	RADAR received signal
$\overline{y}_D$	filtered and downsampled form of demodulated received signal
y_{IQ}	demodulated received signal y_D
y_{M1}	computed I-Q data of Method 1
y_{M2}	computed I-Q data of Method 2
$\overline{y}_D^*$	complex conjugate of $\overline{y}_D$
$\angle$	phase of a complex number

Greek symbols

α_ϕ	high pass filter factor
θ	phase
$\Delta\theta$	phase shift
λ	wavelength
σ	mean RADAR cross-section of the target

1 INTRODUCTION

1.1 Background

During the second world war, radio detection and ranging (RADAR) systems were developed to track the objects and missiles in long-distances. During that time, sound and light detection were the two main options for this purpose. The acoustic detectors were developed in the first half of the 20th century. The light detectors had a very narrow field of view due to its short wavelength, and the acoustic waves did not have enough efficiency. A better perception of the electromagnetic waves affected the technology to invent novel systems for long-range discovery. RADAR systems were developed and significantly impacted the second world war by detecting the airplane and missiles. The concept was sending an electromagnetic wave and taking back the reflection from the target object. The echo signal was analyzed by its features such as amplitude, time of flight (TOF), and phase shift compared with the transmitted signal.

New advancements in both material science and electronics made it possible to design the RADAR concept in a tiny package compared to the first generations. Although the small package means less power and the scanning narrows to short-range detection, the applications were designed for the mm-wave RADAR chips. The RADAR chips were implemented on portable devices such as mobile phones and tablets, which means the enormous potentials of the RADAR systems can be achievable in a pocket-size device.

Exploring the surrounding environment is feasible via active or passive scanners. The most obvious example for the passive scanner is a camera that collects the light and constructs an image. The active scanners are like the RADAR concept. The leading viable solutions for the active scanning are Laser imaging detection and ranging (LIDAR), sound navigation and ranging (SONAR), and RADAR. In all of these methods, a wave is transmitted, and the reflected wave is investigated for extracting particular features. The comparison between these methods are discussed in Chapter 2.1.

Different types of categorizations are defined for RADAR systems. RADAR is classified recording to the RADAR characteristics such as frequency band and antenna type, RADAR functionality, types of the waveform, and other technical characteristics [1]. Recording to this study's application targets, antenna design, and waveform types are the essential features. The antenna design can be divided into multi-receiver channel RADAR and single receivers. The waveform type can classify the RADAR into continuous wave

(CW) or pulsed wave (PW) RADAR. Each of these methods has benefits and drawbacks, which are specified in Chapter 2.2.

The short-range mm-wave 60 GHz RADAR integrated silicon device solutions have emerged recently. By frequency range between 57 GHz to 64 GHz, this RADAR system can provide 7 GHz bandwidth, which is an excellent opportunity to define new applications with reasonable accuracy. This specific bandwidth was utilized for different applications. The target applications with the ability for implementation on the mobile device are expressed as follows:

- Presence and occupancy detection such as people counting, people's actions classification, room automation, and object detection.
- Human-computer interaction (HCI) such as gesture recognition.
- Material detection such as material classification or sense of touch for the robots.
- wearable assistance solution for people with disability or army.
- Vital signs such as heart rate vibration, respiration rate, human body micro-vibration, blood pressure, and glucose level meter.

The RADAR system's primary healthcare applications are respiration and heartbeat rate detection, which is feasible due to this sensor's high sensitivity to the micro-vibrations. The RADAR which is based on the active scanning make it possible to do contactless measurements. Also, the wave can penetrate through the thin non-metallic materials. This sensor's contactless feature has a unique potential for health monitoring both within hospitals and houses.

1.2 Objectives and delimitations

This study concentrates on the vital sign detection ability of the mm-wave RADAR system. The 60 GHz RADAR system of Acconeer company [2] by the Raspberry Pi board [3] is used for data acquisition. This RADAR system has only one transmitter and one receiver for saving more energy and space in portable appliances. The study is limited to short-range vital sign detection with the standard environment in which the target is stationary. For this purpose, RADAR raw data analysis and signal processing were considered, and the accuracy of the system was tested. The discovered object in the RADAR

field of view was divided into two main categories of an alive or non-alive object. For this purpose, the vital sign recognition algorithm is scanning the area and detecting the chest's location. The objectives of the thesis are summarized as follows:

- Setting up the system and data acquisition using RADAR and Raspberry Pi.
- Chest tracking using RADAR data processing.
- Extracting the vital sign information such as respiration, heartbeat rate.
- Using different algorithms for phase unwrapping.
- investigating the potential of the RADAR in case of transmission over different materials.
- Analyzing the accuracy of the results by using a standard measurement device.

1.3 Structure of the thesis

In this thesis, the vital sign detection methods are performed using a 60 GHz RADAR development kit. Chapter 2 is started with comparing RADAR with other alternatives such as SONAR and LIDAR. In the following, the advantages and disadvantages of both CW and PW RADAR are discussed. The mm-wave RADAR's main applications are overviewed, and the previous works related to vital signs and presence detection are explained. Chapter 3 is discussing the RADAR concept and the raw RADAR signal. The signal processing and proposed algorithms for the respiration and heartbeat rate detection are explained in Chapter 4. Chapter 5 focuses on the practical results, and the estimations were acquired using the proposed algorithms. Chapter 6 is making the discussion for the current study and the future work and discuss the accuracy of the results. Finally, a short conclusion is given in Chapter 7.

2 RADAR SYSTEM BENEFITS AND APPLICATIONS

2.1 LIDAR, SONAR or short-range RADAR

For short-range proximity, the most critical sensors are ultrasound, LIDAR, and short-range RADAR. All of these sensors are active and sending a wave and take back the echo signal. Ultrasound sensors employ frequencies from the tenths of kHz to MHz, which depends on the sensor specification. The lower frequencies of ultrasound were used for proximity sensing and similar applications as this study. The higher frequencies can penetrate the body and be used as an imaging system. The LIDAR uses the optical time of flight, and the mm-wave RADAR has a wide variety of frequency bands, but in this study, the focus is on 60 GHz RADAR systems. It is possible to discuss these sensors' differences by analyzing the available sensors' specification and the concept behind the specific frequency range features. The LIDAR system has the lowest wavelength and can obtain the most precise spatial resolution. The maximum detection range of the RADAR is higher than the Ultrasound and LIDAR. The mm-wave RADAR's minimum range detection is small, less than half a millimeter, but the ultrasound sensor chips cannot detect an object in the short-range. Because the miniaturized ultrasound chips use the same area for transmitting and receiving the signal and there has to be a time gap for the ringing after signal transmission. The ringing of the transmitters leads to higher decay time.

The LIDAR and RADAR sensor has a wide field of view. The RADAR signal can penetrate to the non-metal materials. One of the most valuable outcomes of this feature is the RADAR robustness against environmental factors. On the other hand, ultrasound and LIDAR are more sensitive to the environment. The ultrasound sensors are better in range resolution than object speed estimation, and in general, these sensors are the most affordable method for proximity sensing. The RADAR sensor has a tremendous ability both in range and frequency domain, allowing sensing small changes. The LIDAR can have better object characterization due to better spatial resolution, but the system is non-robust against ambient light. It is possible to perform beamforming by designing a multi-receiver channel. In this case, the receivers have to be located with half of the wavelength distance from each other. The ultrasound sensor array occupies a large space, as an example, using a wavelength of 40 kHz leads to 4.3mm distance between the sensors. For the 60 GHz RADAR system, the receivers are located with a 2.5mm distance. All of these benefits of RADAR systems represent it as an essential solution for proximity and ranging.

2.2 Continuous wave or pulsed wave RADAR

The short-range small mm-wave RADAR can be categorized into two main types, the CW and PW RADAR. The CW RADAR is transmitting a continuous electromagnetic wave, and the receiver receives part of the reflections. The comparison of transmitted and received signals can address information about the range and movements of the target. This concept was extended to frequency modulated continuous wave (FMCW) RADAR, in which the frequency is changing periodically over time [4]. The PW RADAR is based on the TOF concept, which detects the time difference between transmission and receiving the echo of the pulsed signal. "Compared to CW RADAR, the main advantage of PW RADAR is the intrinsic immunity to multi-path reflection" [5]. The FMCW RADAR use a continuous transmission, which leads to continuous power consumption. The PW RADAR has its complexity, which is due to fast time signal detection. The electromagnetic waves are traveling with the speed of light, leads to a short TOF. The FMCW RADAR has better doppler resolution than PW RADAR, and on the other, the PW's separate transmitter and receiver do not suffer from the leakage between these elements [4].

2.3 Applications of RADAR on detection of the presence and vital sign

This section focuses on the presence and vital sign detection application of mm-wave RADAR. Yavari et al. [6] investigated occupancy monitoring by using a 2.405 GHz CW RADAR system. The system detected the heart rate and respiration by filtering the signal in particular frequencies. The measurement was done for different body moves such as walking or running, although the vital sign was measured in a stable condition. Lurz et al. [7] presented a 24 GHz doppler RADAR system for presence and respiration detection. By using intermittently measuring, the power consumption was significantly reduced compared to CW RADAR. The measurement was arranged by placing the RADAR system at a precise distance from the target, and the proposed system was able to detect the respiration. Baird et al. [8] introduced an algorithm for occupancy detection in a room using principal component analysis (PCA). The measurement was taken with ultra wideband (UWB) RADAR in an empty room and a room with one or two persons. The signal energy can be different in various bins, and the highest energy peaks show a strong echo at a certain distance so that the occupancy detection would be achievable.

Santra et al. [9] proposed a RADAR system for occupancy sensing applications by using

a 60 GHz FMCW RADAR sensor. The experiment was done for different human body movement classes such as macro doppler (walking and running), micro doppler (working on a computer), and vital doppler (heartbeat and respiration). The result claimed an absolute presence detection, but the vital sign detection was performed in sitting or standing idle case. The vital sign was calculated by interferometric techniques and estimated the heartbeat rate. Santra et al. [10] proposed a multi-channel FMCW RADAR system with two receivers and two transmitters, which was able to construct a two-dimensional image with a specific field of view. By using multiple-input multiple-output (MIMO), which is an advanced phased array system, the RADAR system can create an image in the horizontal plane and can identify the people and objects in a particular field of view. Also, because of the great potential of FMCW RADAR in the frequency domain, the system was able to identify the heartbeat rate and respiration individually by using proper filters.

Many studies are explicitly focussing on the noncontact heartbeat rate and respiration detection [11–14]. Zakrzewski et al. [11] proposed a novel method for heartbeat rate detection. The robustness of the measurements was evaluated for different angles between the sensor and the human chest. Alizadeh et al. [12] proposed a remote heartbeat rate sensing using a 77 GHz RADAR system. The results were measured by facing the RADAR system by a distance to the target person to simulate sleep monitoring. Hu et al. [13] developed an algorithm for measuring the heart rate variation and respiration using wavelet transform (WT) and empirical mode decomposition. The algorithm was tested for both the simulated target and the human body. The respiration has an artifact in heartbeat rate detection, but the algorithm was able to separate these two features. The most common solution is a narrowband filter recording to the target feature, which has limited ability. Zakrzewski and Vanhala [14] developed an algorithm for dividing these two features utilizing complex-valued Independent Component Analysis.

3 RADAR SIGNAL PROCESSING

3.1 RADAR system overview

The electromagnetic wave transmits from the RADAR and hits the target. The transmitted wave characteristics and the target object features can estimate the proportion of the wave return to the RADAR system. The time of flight plays a significant rule in signal attenuation. Furthermore, the RADAR cross-section (RCS) of the target affects the echo signal. The RCS depends on the size, shape, and material properties of the target. Consequently, the metal objects can be detected from longer distances compared to the object with the same size by non-metal material properties. The received power is presented as [15]

$$P_r = \frac{P_t G_t G_r \lambda^2 \sigma}{(4\pi)^3 R_0^4} \tag{1}$$

where P_r is the peak received power, P_t is the transmitted power, G_t is the gain of the antenna in the transmitter , G_r is the gain of the antenna in the receiver, λ is the carrier wavelength, σ is the mean RCS of the target and R_0 is the range from the RADAR to the target.

The active PW RADAR is based on the TOF concept, which measures the electromagnetic wave's travel time between transmission and receiving the signal. The range sample, R_0, is calculated as [15]

$$R_0 = \frac{c\Delta T}{2} \tag{2}$$

where c is the speed of light, and ΔT is TOF. The ΔT is the period between sending and receiving the RADAR wave. It is obtainable using matched filters, which applies the convolution of received wave and time-shifted transmitted wave [16]. The time-shifting makes it possible to estimate the range or fast-time samples.

3.2 Pulsed wave RADAR waveform

Modeling of the RADAR waveforms can make a better understanding of the concept. A summary of the modeling is available in the following text; more expanded derivation is in [15]. The PW RADAR can transmit the pulse with the general form as follows:

$$x(t) = A(t)\cos(2\pi f_0 t + \theta) = Re\Big\{\big(A(t)\exp(j\theta)\big)\exp(2\pi j f_0 t)\Big\} \tag{3}$$

where x is the RADAR transmitted pulse, t is time, A is the Gaussian envelope, $A(t) = exp(-t^2/2\lambda^2)$ [17], θ is the phase, and f_0 is the RADAR's carrier frequency which in this study indicates f_0 = 60 GHz. Therefore the amplitude of the cosine signal is changing in accordance with the Gaussian envelope, and this modulated signal is a pulse wave. This pulse was expressed as a vector with the amplitude of A and the phase of θ. This wave is hitting the target and travel back to the receiver and is modeled as

$$y(t) = A'(t)\cos\left[2\pi f_0\Big(t - \frac{2R_0}{c}\Big) + \theta\right]$$

$$= Re\left\{A'(t)\exp\left[j\Big(\theta - \frac{4\pi}{\lambda}R_0\Big)\right]\exp\left(2\pi j f_0 t\right)\right\} \tag{4}$$

where y is the RADAR received pulse, t is time, A'(t) is the envelope of the received signal, R_0 is the range of the target, and λ is the wavelength. The amplitude has changed, and the wave is delayed by $\Delta T = 2R_0/c$. Also, the phase of the received pulse is shifted by $\Delta\theta = -4\pi R_0/\lambda$ radians [15]. In Eq. 4, $A'(t)$ is the multiplication of a constant with the delayed envelope which means, $A'(t) = (Constant) \times A(t - 2R_0/c)$ [16]. This constant represent the loss of power which is the ratio of P_r and P_t, as it was demonstrated in Eq. 1.

3.3 In-phase-quadrature detector

The pulse in the receiver splits into two channels. The procedure is demonstrated in Fig. 1 [15], which combine the signal with reference signals to produce the in-phase (I) channel, and quadrature (Q) channel. Using complex channels makes it possible to estimate the received signal's amplitude and phase compared to the transmitted signal. The received signal is mixed with two reference oscillators with a 90-degree phase shift between them. The mixed signals were low pass filtered to remove the sum frequency term. If there was just one mixer, the total phase and amplitude could not be distinguished. The coherent or in-phase-quadrature (I-Q) detector uses the complex output, and by this concept, it is possible to calculate phase and amplitude separately [15].

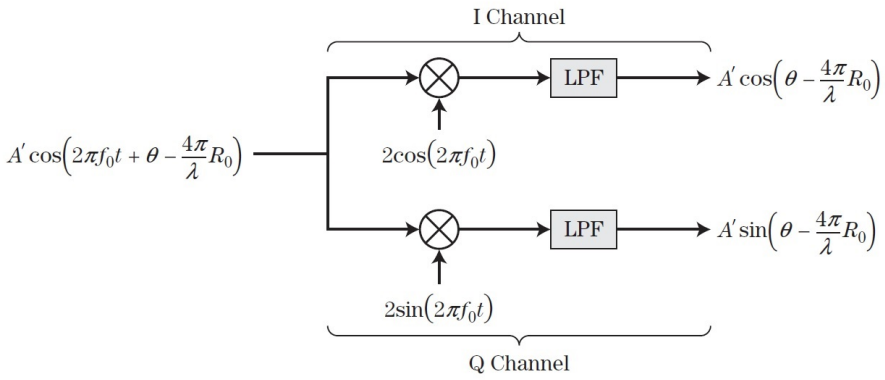

Figure 1. In-phase-quadrature (I-Q) Detector. [15]

3.4 RADAR raw data

The method, which is presented in Fig. 1 is the I-Q demodulation. The RADAR received signal $y(t)$ in Eq. 4, is demodulated to $A'(t)exp(j\theta)$,and it means the carrier frequency is excluded [17]. The I-Q demodulated signal has a real part, I, and an imaginary part, Q. The I-Q demodulation is utilized to the received raw data $y(t)$ and produced the I-Q signal y_{IQ} as

$$y_{IQ}[s,d] = I[s,d] + jQ[s,d] \tag{5}$$

where s is the slow time index or sweep number ,and d is fast time index or range index. The real and imaginary part of the y_{IQ} is the I and Q channel output of the I-Q demodulator, respectively, which is demonstrated in Fig.1. For each selected range, there is a time expectation that can be calculated from Eq. 2, which corresponds to a particular matching filter. Therefore, one y_{IQ} is estimated for each range samples, and the estimations are updated in the time domain, which corresponds to different sweep numbers. The I-Q signal is represented as Fig. 2 [18]. Each of the blocks in Fig. 2(a) represents a complex number for a specific distance to the sensor. The fast time sampling interval is T_s, and L is the number of range samples in each sweep. This scenario was renewed and produced another dimension to the data as slow time information. Pulse repetition frequency (PRF) is the numbers of the transmitted signal per second, and the pulse repetition interval (PRI) is the time between sweeps. Fig. 2(b) [18] shows the fast and slow time RADAR data.

In Fig. 2(a), each of the samples corresponds to a particular range. The number of range samples depends on the step length, which refers to range resolution and the range scanning region. The range samples are modeled as

$$R_0 = a + d \times st, a < R_0 < b, \tag{6}$$

where R_0 is the range sample, a is the lower limit of the range, b is the upper limit of the range, st is the step length ,and d is an index to range samples, $0 < d < L$. For example, if the range scanning region is between $0.4m$ to $0.6m$, the first range sample corresponds to $0.4m$, and the last range sample belongs to $0.6m$. If the step length is $0.48mm$, it means scanning the radar field of view from $0.4m$ to $0.6m$ with the steps of $0.48mm$, such as $400mm, 400.48mm, 400.96, ...$ After I-Q demodulation, a complex number is provided for each of the data samples. One sweep means a set of fast time or range samples. Fig. 1(b) shows the repeated sweeps which construct the slow time axis.

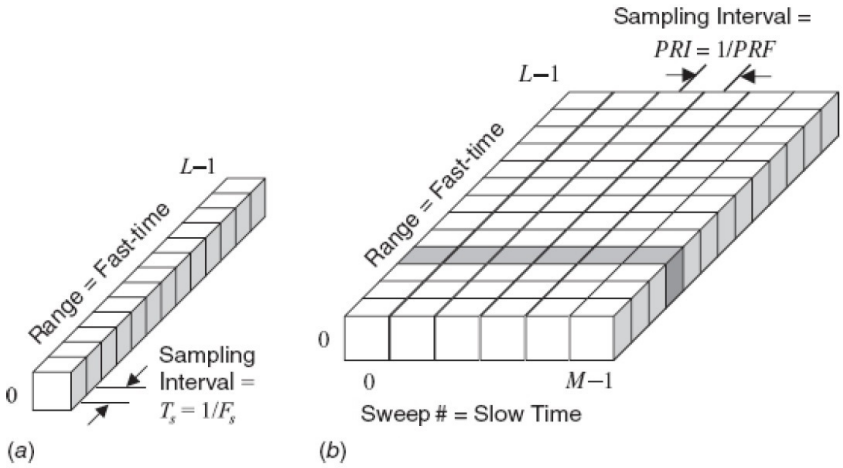

Figure 2. (a) Fast time samples of one sweep which contains L samples over the range, (b) Fast and slow time for M sweeps. Each of the fast time samples corresponds to a specific range, representing the range information, which is varying in time through the slow time dimension [18].

4 PROPOSED METHODS

4.1 Vital sign detection methods

The target can be detected by calculating the I-Q signal's amplitude in the RADAR field of view. Because a reflected signal with high amplitude in a specific range confirms the presence of an object in that particular range. In this study, different methods were applied for extracting the desired data within each sweep. Each sweep consists of L different range data and different methods employed to extract a phase information for each sweep. According to Fig. 2(a), different methods obtain one phase data instead of the whole of the fast-time samples in each sweep. For estimating the phase information, the following three methods are described:

- Method 1 is considering the specific range sample with the highest signal amplitude.
- Method 2 is based on averaging the phase information of all of the range samples.
- Method 3 is based on the Acconeer evaluation software and is a reference method [19].

4.2 Phase estimation

Method 1 is adopting the echo signal's maximum amplitude and estimate the phase of that specific range. Recording to the particular use case of this setup, it is considered that the range with the highest amplitude is a representative of the human body. In Eq. 6 for each sweep number (s), there are L numbers of complex data. Method 1 starts by finding the maximum amplitude of these complex numbers for each sweep and selecting one complex number with the highest amplitude. Method 1 estimate the I-Q signal as

$$y_{M1}[s] = y_{IQ}[s, d_{peak}] = I[s, d_{peak}] + jQ[s, d_{peak}] \tag{7}$$

Where y_{M1} is the computed I-Q data of Method 1, y_{IQ} is the initial I-Q signal, s is the slow time index or sweep number, d_{peak} is the range index with the highest amplitude within a sweep, and d is the fast time index or range index. Method 1 has the potential to detect multiple objects and extract vital signs from different ranges. Because in Method 1, the I-Q data was extracted from the range data with the highest signal amplitude, and

it can be extended to find multiple peaks in the range data. In this case, the algorithm can find, for example, two different peaks that correspond to two different alive people.

Method 2 uses the whole of the I-Q data in each sweep and summing up these complex numbers for each sweep. Thus, a complex number is computed in each sweep as

$$y_{M2}[s] = \sum_{d=0}^{L-1} y_{IQ}[s,d] = \sum_{d=0}^{L-1} I[s,d] + j \sum_{d=0}^{L-1} Q[s,d] \tag{8}$$

Where y_{M2} is the computed I-Q data of Method 2, y_{IQ} is the initial I-Q signal, s is the slow time index or sweep number, and d is the fast time index or range number. Method 2 is the most simplified algorithm that sums all of the variations in each sweep and is designed to show a simplified method's accuracy, which has the least computation cost.

The I-Q data extracted with Method 1 and Method 2 provide a time series of complex data samples. For each sweep, phase information was estimated, which means M number of phase data. This phase information computed from the I-Q data must be unwrapped, which means the phase information with a sudden significant change must be shifted. Therefore, the unwrapping can remove the sudden changes, and the final phase information is a smooth signal. The algorithm implemented in $unwrap$ function in Matlab can shift the phase information [20]. The jump threshold value has the default value, which is π. For calculating the phase information, arctangent demodulation was tested, and the result was unwrapped, but discontinuity may happen [21]. Thus, estimating the I-Q data phase and unwrapping the results with Matlab $unwrap$ function can cause some discontinuity in the output.

In Method 1 and Method 2, one I-Q data was extracted for each sweep, which means the range information is eliminated. It means recording to Eq. 7,8 the I-Q data loses its relevance to range and is simply relevant to the sweep index. Thus, the I-Q data for each sweep is a representative of the whole of the fast time samples. Instead of estimating phase and applying Matlab $unwrap$ function, phase extraction was determined with a different algorithm as [21]

$$\theta[s] = \sum_{k=1}^{s} \frac{I[k]\{Q[k] - Q[k-1]\} - \{I[k] - I[k-1]\}Q[k]}{I[k]^2 + Q[k]^2}, \tag{9}$$

where θ is the phase for one sweep, k is the sweep number counter, s is the sweep number, I is the real part, and Q is the imaginary part of y_{M1} or y_{M2} (depends on which method was applying). This method uses the derivative of the arctangent demodulation, and in the case of online data processing, the phase can be unwrapped sweep by sweep. The chest

displacement is obtainable by modifying the phase variation. The chest displacement is representing the changes in range data. The phase information was modified into the displacement, using $\lambda = c/f = 4.99654mm$. As an example, for 2π phase changes, the displacement is calculated by $R_0 = \lambda\Delta\theta/4\pi \approx 2.5mm$.

The Method 3 is starting by downsampling, and next, it is followed by a noise reduction applying a low pass filter to the time dimension. The next step is phase estimation, which was calculated by [19]

$$\theta[s] = \alpha_\theta\theta[s-1] + \angle\Big\{\sum_{d=0}^{L-1}\overline{y}_D[s,d]\overline{y}_D^*[s-1,d]\Big\}, \tag{10}$$

where θ is the phase, $\overline{y}_D[s,d]$ is filtered and downsampled for of $y_{IQ}[s,d]$, α_θ is a high pass filter factor, L is the number of fast time samples, s is sweep index, d is range index, $\angle$ is the phase of complex number, and $\overline{y}_D^*$ is the complex conjugate of $\overline{y}_D$. For each sweep, one phase data was calculated and was used for further analysis.

After obtaining the phase data for each sweep, the fast Fourier transform (FFT) can extract the frequency domain information. The typical respiration rate is between 8 to 24 beats per minute, and the heartbeat rate in rest position can change between 50 to 90 beats per minute [22]. It means the highest rest respiration rate in the frequency domain is $0.4Hz$, and the lowest rest heartbeat rate is $0.8Hz$. Thus, the harmonics of respiration can overlap with heartbeat rate frequency [23].

The proposed heartbeat variation algorithm by Hu et al. [13] was based on wavelet transform and ensemble empirical mode decomposition (EEMD). The empirical mode decomposition (EMD) uses the signal's maximum and minimum points to make higher and lower envelopes. The mean value of these envelopes can estimate the signal's lower frequency component, and the high-frequency component can be estimated by subtracting this mean value from the signal [24]. This procedure is repeating to obtain more components from the signal. Due to the vulnerability of EMD in the presence of noise, the EEMD was developed. In this method, the intrinsic mode functions were calculated after adding white noise to the signal [24]. The WT was estimated as a concept obtained by scalable windowing of the Fourier transform [25]. During this procedure, the signal's high and low-frequency components were extracted by the signal's long or short windowing.

Computational complexity of different phase estimation methods

The phase estimated by Method 1 and Method 2 requires phase unwrapping to remove the

discontinuities, as it was shown in fig. 3. The estimated phase by Method 3 does not have a discontinuity, and phase unwrapping is unnecessary. According to Eq. 10 in Method 3, an angle was estimated for each sweep, which was based on the multiplication between $\overline{y}_D$ and $\overline{y}_D^*$. This angle is representative of the phase variation between two sweeps. Thus the final phase was calculated by summing phase change with the phase, which was calculated from the previous sweep. Method 1, shown in Eq. 7, is based on finding the maximum signal amplitude in each sweep. Thus the signal amplitude was estimated for each sweep, and the I-Q value of that specific range sample was considered for the phase unwrapping. Method 2, , presented in Eq. 8, requires the summation of all of the range samples in each sweep. Hence the Method 1 and Method 2 has less computational cost compared with Method 3. According to Matlab's elapsed time for each method, Method 1 has approximately 8% more computational cost than Method 2. Also, Method 3 has around 23% higher computational cost than Method 2.

4.3 Respiration and heartbeat rate detection

Fig. 3 shows the proposed setup for heartbeat and respiration detection. The procedure was started by phase calculation by performing Method 1, Method 2, and Method 3 on calibrated I-Q signal. The phase data was unwrapped, and by implementing WT, the respiration rate was estimated employing WT's approximation components. The WT's detail components are representative of the heart movements (because it has higher frequency), and the approximation is selected as a representative of the respiration (due to the lower frequency). Three different digital signal processing (DSP) was used to calculate the heartbeat rate. The DSP 1 consists of WT, detecting the relevant details, moving average filter (MAF) that reconstructs the signal, and peak detection, which finds the peak to calculate the heartbeat rate. The DSP 2 is created by using WT, EEMD, MAF, and peak detection. DSP 3 is the only DSP that is not based on WT and starts by a bandpass filter from $0.7Hz$ to $2.5Hz$. This frequency corresponds to $42beats/min$ and $150beats/min$, respectively. Then the MAF has reconstructed the signal, and peak detection could find the exact location of the peaks in the time domain. The final heartbeat rate in all DSPs was calculated using the average value of the period between the peaks and converting it into beats per minute.

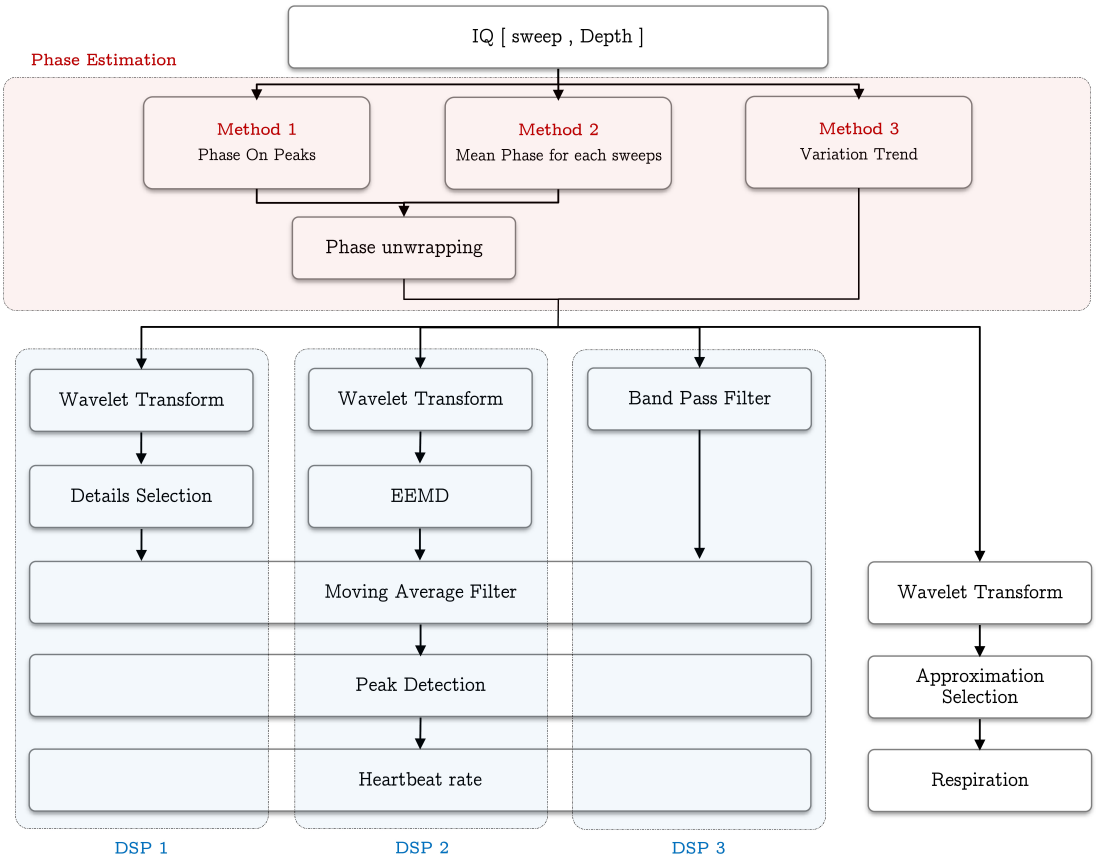

Figure 3. The proposed setup for vital sign detecion.

5 EXPERIMENTS AND RESULTS

5.1 Measuring the primary I-Q signal

The raw data was obtained by transmitting signals and reading the echo signal as in Eq. 4. The final data samples, as demonstrated in Fig.2, contain I-Q data, which has both amplitude and phase. Each of these data samples is related to one transmitted and received pulse. These measurements were optimized by the pulse width and transmitted signal gain. Without considering phase information, the amplitude data can provide a rough estimation of the region of interest. The I-Q signal can provide better information about the object's micro-vibrations and is the data with more sensitivity. The I-Q signal contains the phase information, and the small changes in the object can have a significant impact on the phase response.

The raw I-Q data is captured based on the algorithms of the Radar software [19]. Because the first step is raw data calibration, which was already done in the software algorithm. It indicates that the I and Q data was calibrated to have a 90-degree phase difference. Hence, The I-Q data in Fig. 3 is the calibrated data.

A Python exploration tool software accompanies the hardware setup with a stable graphic unit interface (GUI) [19]. It is possible to capture the data with several sensors and use the desired configuration to scan a specific range. Using the exploration tool and setting the configurations for scanning specific range and particular pulse length, it would be possible to do the measurements. These measurements were saved, and the data was used for further analysis in other software such as Matlab.

5.2 Description of experiments and experiment setup

This study uses the A111 RADAR sensor [2], which is a single channel RADAR; therefore, it only has one transmitter and one receiver. The Raspberry Pi 4 with the Raspbian operating system was adopted for capturing the data, and the signal processing part for generating the raw I-Q data was done in Python by the producer. The I-Q data were transferred to Matlab for further analysis.

A mock-up was printed with a 3D printer, and the sensors were placed on the corners of the tablet-like device. A radome or RADAR dome is the RADAR protector [26], and in

this study, it indicates the front layer on top of the RADAR sensor. The distance between the RADAR chip and the radome and the radome's thickness also must be optimized. The permittivity of the radome is the main factor that affects this optimization task. Besides, it depends on the target application. In this study, the goal is a commercial product in which miniaturization plays a significant role. It has to be tested in practice to find the best optimization solution. Data acquisition was made by using a free space RADAR without implementing a radome. In this case, the results are not dependent on the radome design, and this step can be done in product development.

A person was sitting on a chair in the rest mode, and the sensor was facing the chest with roughly $R = 40cm$ distance. During this research, the robustness against the movement was not studied, so the data was captured with minimum artifacts. As a reference device, Bittium Faros 180 electrocardiogram [27] was used to capture the heart rate variation simultaneously.

The data was captured by the RADAR setup in three different RADAR positions. Fig. 4 demonstrates the RADAR positions and the general path of the RADAR wave, which provides the desired data. The main target application is fixing the RADAR system in a fixed position, which is shown in Fig. 4 (Dataset 1). Most of the data set are captured in the RADAR fixed position to make a reasonable judgment about the system's accuracy in this configuration. The RADAR was fixed on a table, and the distance between RADAR and chest was roughly $50cm$. In Fig. 4 (Dataset 2), the RADAR setup was held in hand, and the RADAR field of view was covered with a wall with roughly $55cm$ distance. Lastly, in Fig. 4 (Dataset 3), the RADAR is mounted on the chest, and it is faced to the outside. In this setup, there has to be a fixed position object which covers the RADAR field of view. In this experiment, the RADAR was faced with a wall with an approximate distance of $75cm$.

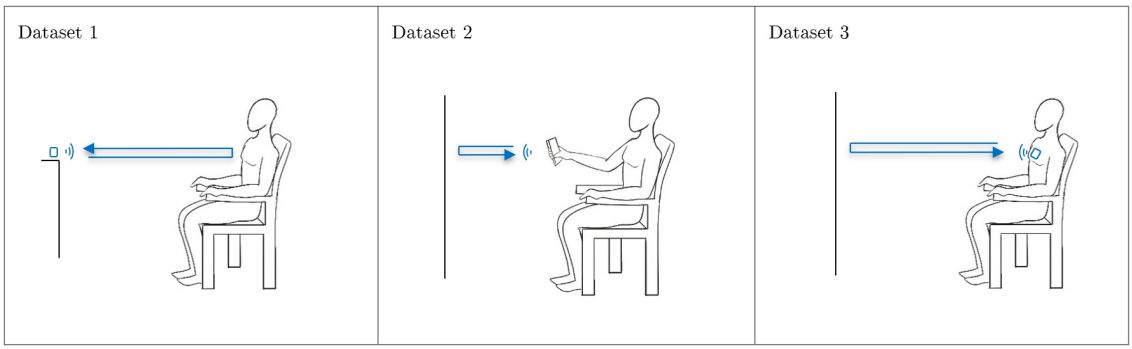

Figure 4. Various RADAR positions give different datasets.

The dataset features are expressed in Table 1, which shows different RADAR positions, the number of data, and the scanned range for each of the datasets. The scanned range describes the specific ranges which were scanned by RADAR. The step length for all of the datasets is $0.48mm$, which confirms the range resolution. The step length specifies the number of range data in one sweep. Thus, The L in Fig. 2(a) depends on two factors, the scanned range, and step length. The received gain was 0.5, and all of the datasets were captured by profile number 2 recording to the RADAR software. This profile makes a balance between signal strength and range resolution. The update rate for the whole of the experiments was set at $80Hz$.

Table 1. The dataset features and different RADAR positions.

Dataset	RADAR position	Number of Data	Scanned range (m)
1	Fixed on a table	32	0.4 - 0.6
2	In hand	7	0.4 - 0.7
3	Mounted on chest	4	0.6 - 1.0

The Dataset 1 consists of four scenarios, which are represented in Table 2 and in Fig. 5. These classes are designed to investigate RADAR's potential in measuring the vital signs over different materials. . Approximately half of the Dataset 1 was captured for free space, with a naked chest faced to the RADAR. The first transmission scenario was wearing winter clothes, which was a thick shirt and a winter jacket. The other situation was a glass layer with a thickness of $4mm$ with a $1cm$ distance from the RADAR surface. Finally, the combination of the glass layer and winter clothes was applied to form a more complicated condition.

Table 2. Different transmission scenarios for Dataset 1.

Dataset	Transmission scenario	Number of Data
1-1	Free space	18
1-2	With winter clothes	3
1-3	With glass layer	9
1-4	With glass layer and clothes	4

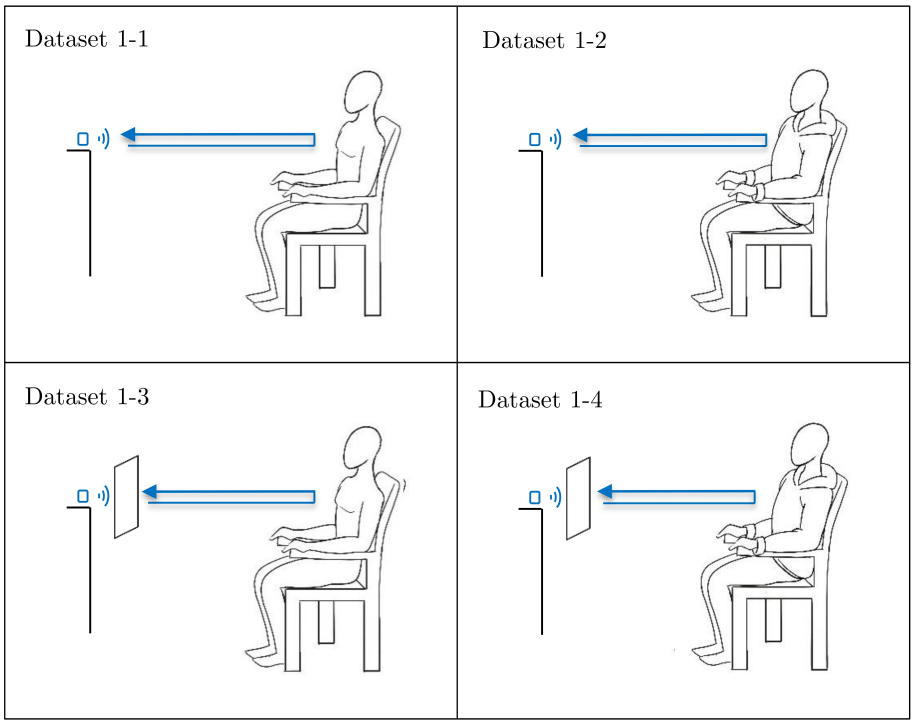

Figure 5. Different transmission scenarios for the RADAR fixed position.

5.3 Extracting phase using proposed methods

The data was captured by RADAR, and the measured data was transferred to Matlab software for further analysis. The phase information was extracted using different phase estimation methods, as shown in Fig. 3. An example of phase data for Dataset 1-1 is illustrated in Fig. 6, which includes different phase-detection methods. The first 40 seconds of the data were captured in the rest position with normal breathing, but after 40 seconds, the breath was held to demonstrate the heart-related impact individually. The purpose of this signal representation is to show the displacement ratio between respiration and heart rate. The respiration has approximately $3.5mm$ displacement, although the heart-related displacement is approximately $0.2mm$. Although the step length for the measurements was $0.48mm$, it was possible to detect smaller displacements. The detected displacement is less than step length because the I-Q data and phase-detection were employed, increasing the detection resolution. After visualizing the whole of the datasets, it was conceivable to observe the confidence of Method 3 comparing with other methods. However, each of the methods has a negative and positive side, which are discussed in chapter 6. The phase data for all of the different transmission scenarios of Dataset 1 are approximately the same as Fig. 6. It is not possible to discuss the difference between transmission scenarios just

by showing the signal shape. Therefore a detailed analysis was done in chapter 5.5.

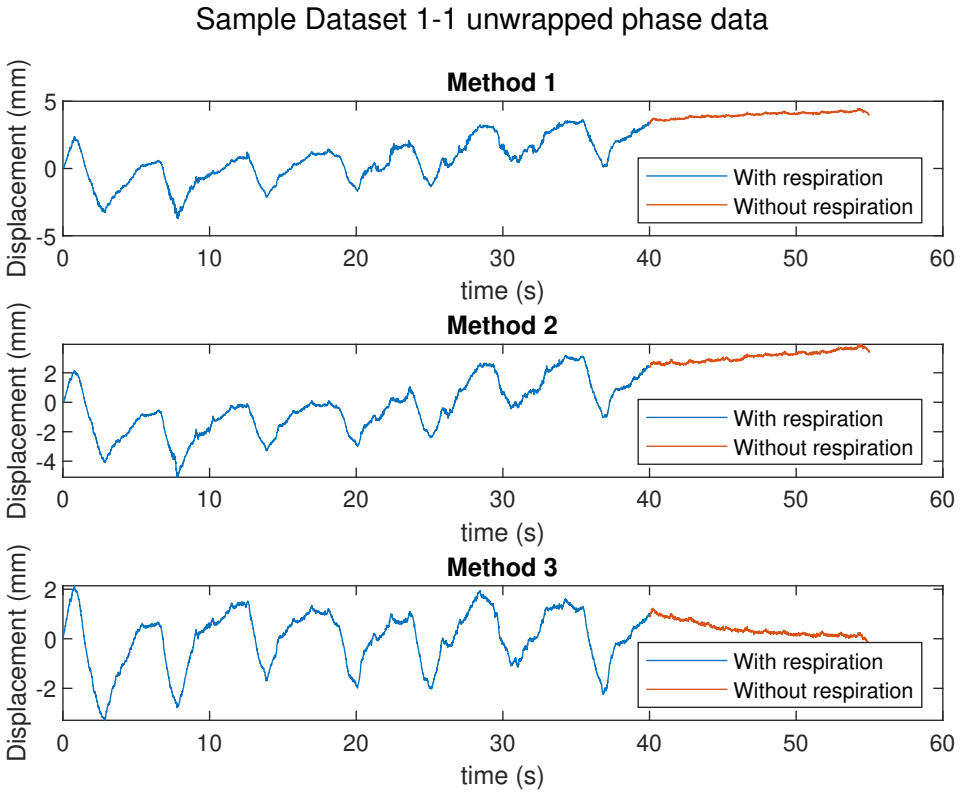

Figure 6. An example of Dataset 1-1 in which the phase estimation was done using three different methods such as Method 1, Method 2, and Method 3. The data was captured for the RADAR fixed position and the naked chest. The first part of the data (demonstrated in blue color) have both respiration and heartbeat rate. The red part of the plot was captured without breathing and was formed by the heartbeat rate.

The phase data for Dataset 2 by applying different phase estimation methods are demonstrated in Fig. 7. Compared to the signals in Fig. 6, the respiration data is eliminated, and the displacement is mainly because of heart rate and body mechanical vibrations. The respiration feature was eliminated because the setup was held in hand. As a consequence, Dataset 2 does not carry reliable information about respiration.

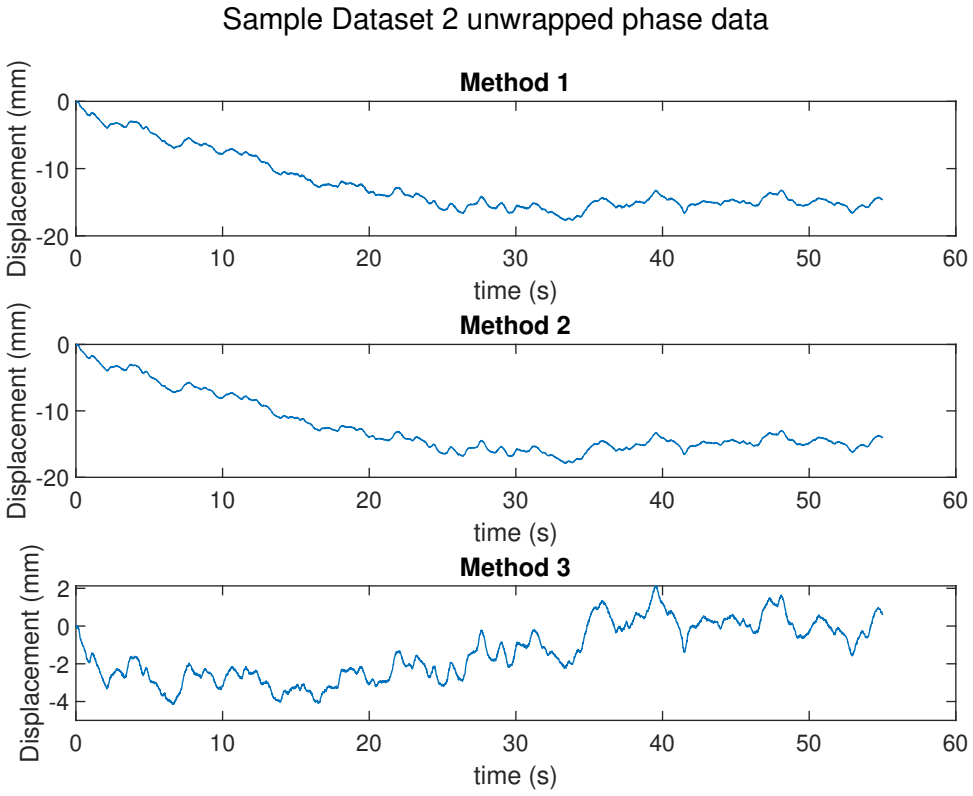

Figure 7. An example of Dataset 2 in which the phase estimation was done using three different methods, such as Method 1, Method 2, and Method 3. During data capturing, the RADAR was holden in hand, and it was facing the wall.

Fig. 8 shows an example of Dataset 3 in which the radar was mounted on the chest. The experiments of Dataset 3 were conducted similarly to Dataset 1, which means 40 seconds of normal breathing, and after 40 seconds, it was without respiration.

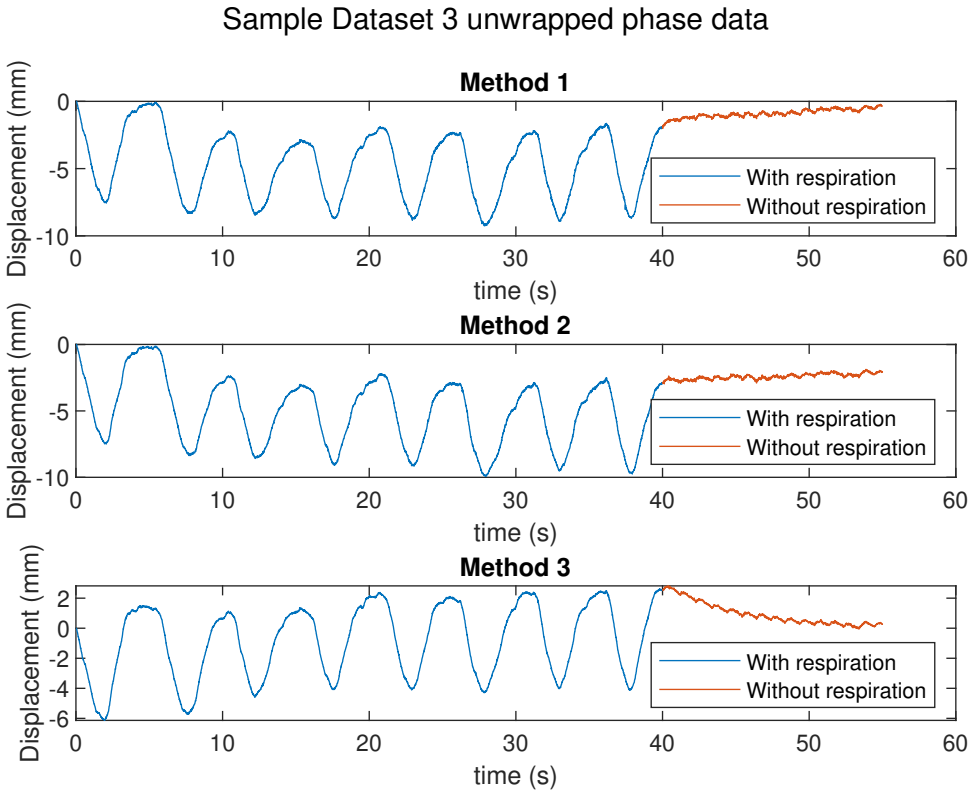

Figure 8. An example of Dataset 3 in which the phase estimation was done using three different methods, such as Method 1, Method 2, and Method 3. During capturing the data, the RADAR was mounted on the chest, and it was faced with the wall. The first part of the data (demonstrated in blue color) have both respiration and heartbeat rate. The red part of the plot was captured without breathing and was formed by the heartbeat rate.

5.4 Extracting the respiration

The target vital signs of this study are respiration and heartbeat rate. The first stage is extracting the respiration from the signal. After testing different wavelet filters, the WT with the Symlet6 wavelet shape, and six layers of decomposition were used in Matlab. The WT by enforcing the wavelet shape to different time bands of the original signal, extract the signal details. An example of this transform is illustrated in Fig. 9, which is based on Dataset 1-1. The approximation at level six represents respiration, and the details at levels 5 and 6 carry heart rate information. The original signal can be reconstructed by combining the approximation at level 6 with all the details from levels 1 to 6.

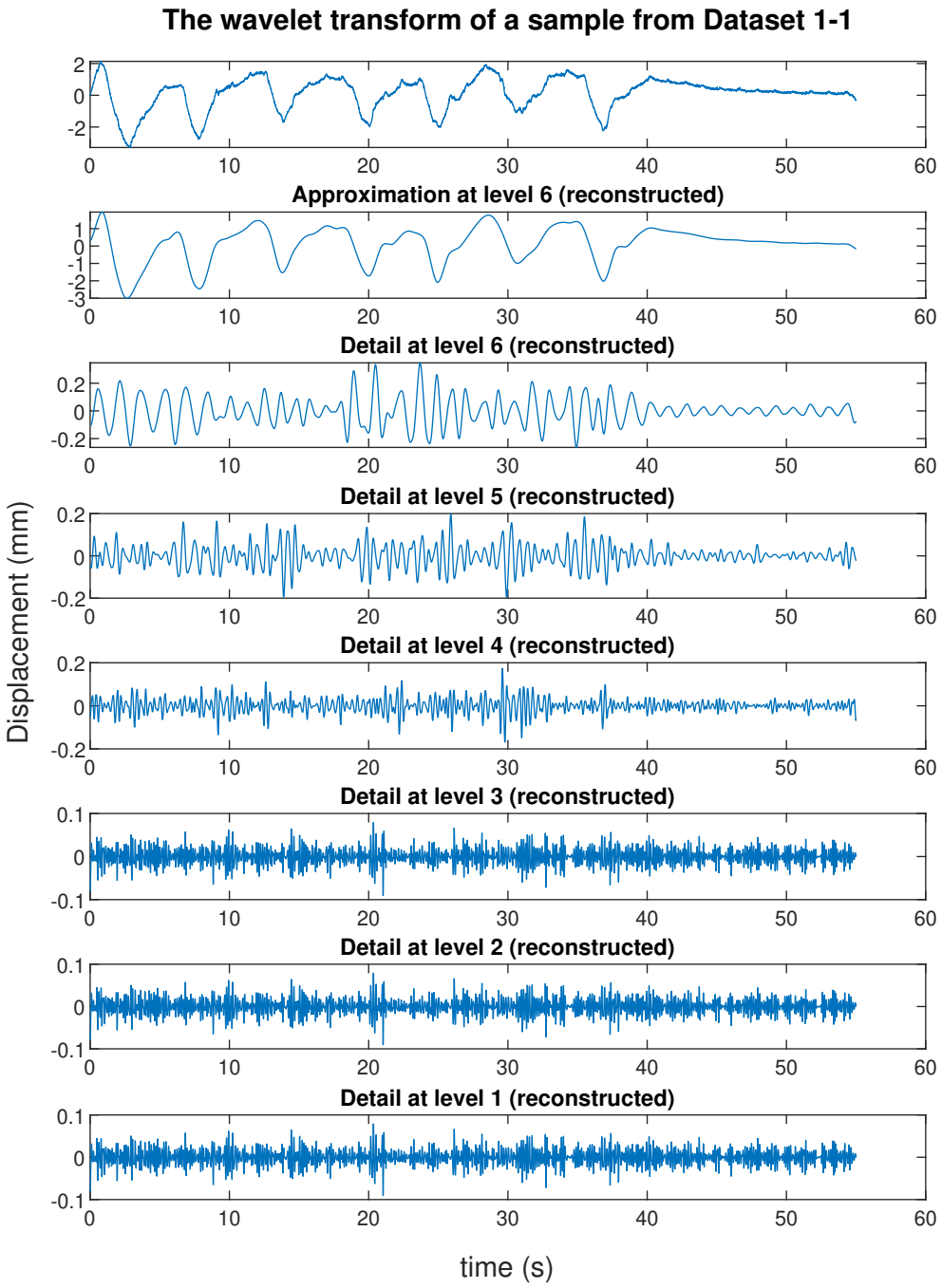

Figure 9. The WT of a sample data from Dataset 1-1. Symlet 6 wavelet with six layers of decomposition, was used to split the phase data.

5.5 Accuracy of the results

The heartbeat rate was calculated using different methods for phase extracting and also different DSPs for signal processing. Fig. 10 shows the accuracy of each of the methods in the form of a boxplot. This method of representing the results can express the accuracy variations recording to different DSPs. The red lines show the median, the lower edge of the box means the 25% percentile, and the higher edge presents the 75% percentile. The lines presented with black lines show the whisker, and the red plus shapes show the outliers. In Matlab, the default value for whisker replies to almost $\pm 2.7\sigma$ and 99.3% coverage if the data are normally distributed [28]. Thus, any data out of this region was considered an outlier. All of the outliers refer to Dataset 2, in which the setup was held in hand. Therefore, because of the larger mechanical hand movements, the results have lower accuracy. However, the difference between the results are reasonable, and these outlier data are not removed from the datasets.

The highest accuracy corresponds to the combination of Method 3 and DSP 3, in which the accuracy of most of the measurements are located in a high number comparing with other DSPs. The combination of Method 3 and DSP 3 has the highest median accuracy of 96.22%. The lowest median accuracy is the combination of Method 1 and DSP 1, with 93.73% median accuracy. The median accuracy for Method 2 is 94.2% for DSP 2 and $94.7\%$for DSP 3.

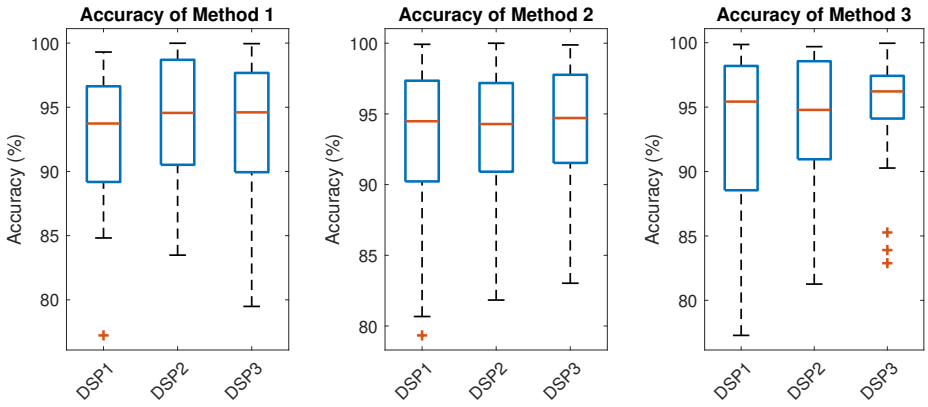

Figure 10. Comparison between the accuracy of different phase estimation methods and DSPs.

The combination of Method 3 and DSP 3 has the best accuracy and repeatability comparing with other combinations. The system's accuracy was tested using a standard ECG device, and it is proper to show the results of ECG and RADAR in the same plot to obtain

a better perception of the waveforms. Fig. 11 shows an example of the RADAR phase variation for the filtered data using combinations of Method 3 and DSP 3, and ECG in the same time domain.

The example of Dataset 2 and Dataset 3 phase variation and filtered data using Method 3 and DSP 3 are illustrated in Fig. 12 and Fig. 13, respectively. The amplitude of the filtered signal for Dataset 2 is higher than the other two datasets because the heart-related movements are captured while the setup was held in hand. In this scenario, the amplitude of the signal can be affected by the direction of the device and the hand's posture.

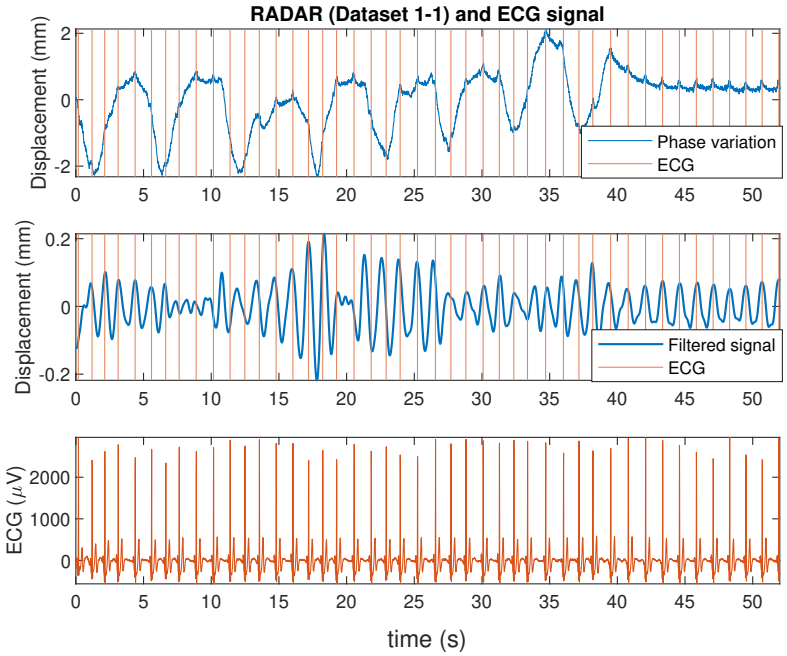

Figure 11. Comparison between the RADAR and ECG signal for a sample from Dataset 1-1.

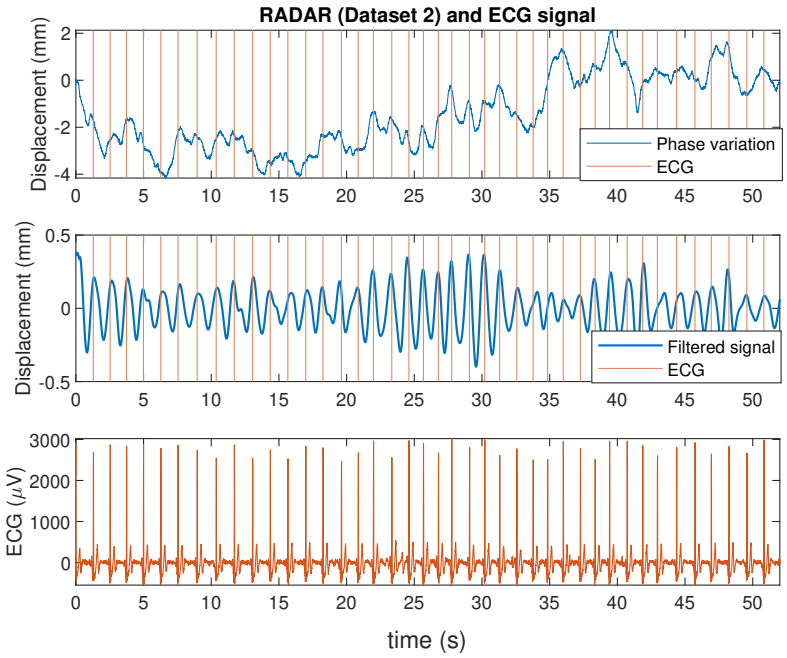

Figure 12. Comparison between the RADAR and ECG signal for a sample from Dataset 2.

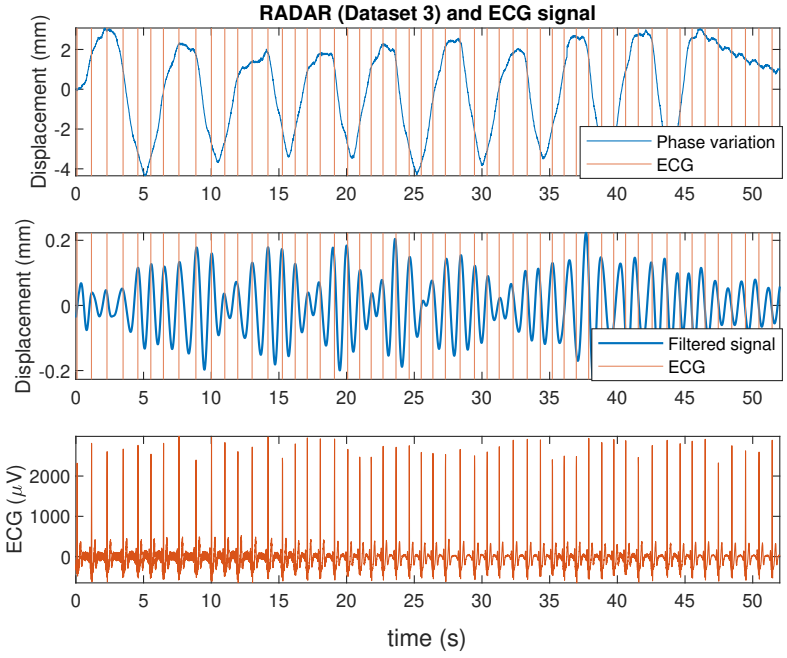

Figure 13. Comparison between the RADAR and ECG signal for a sample from Dataset 3.

The transmission scenarios and different RADAR locations affect the accuracy of the measurements, as illustrated in Fig. 14, and the results are presented in Table 3. Different RADAR locations are represented in different colors, and the tolerance of the accuracy for different measurements is demonstrated with the error bars. The calculation was done using Method 3 for phase extraction and DSP 3 for the signal processing based on filtering.

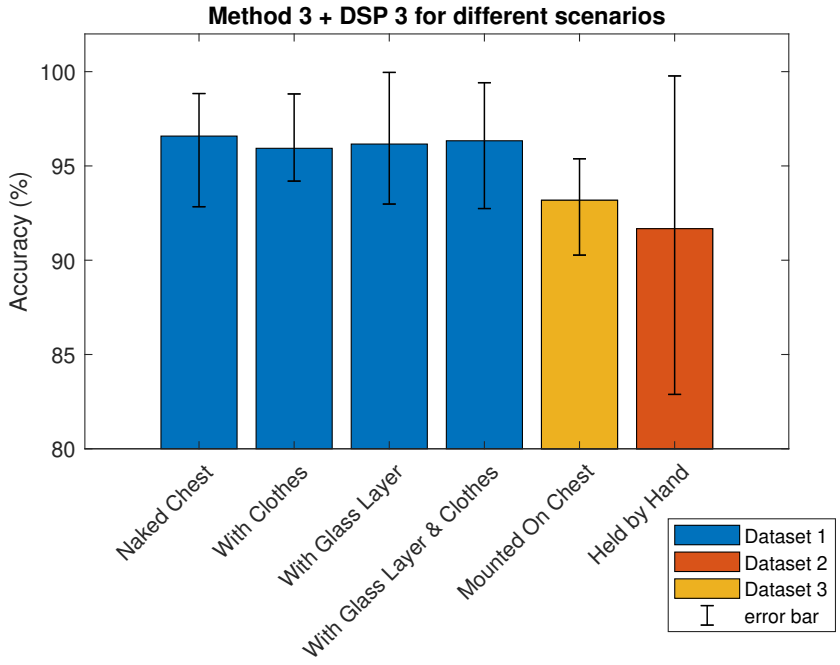

Figure 14. Comparison between the accuracy of Method 3 and DSP 3 for different RADAR positions and RADAR transmission scenarios.

Table 3. Accuracy of Method 3 and DSP 3 for different RADAR positions and RADAR transmission scenarios.

Dataset	Transmission scenario	Accuracy (%)	Accuracy deviation (%)
1-1	Free space	96.5	5.9
1-2	With winter clothes	95.9	4.6
1-3	With glass layer	96.1	6.9
1-4	With glass layer and clothes	96.3	6.6
2	Held in hand	91.6	16.8
3	Mounted on the chest	93.1	5.1

The agreement between two clinical methods can be examined using Bland and Altman visualization technique [29]. It is illustrated in Fig. 15, which displays the agreement between RADAR heart rate detection and a standard ECG system. The horizontal axis shows the average heartbeat rate by ECG and RADAR system, and the vertical axis represents the difference between the two methods (RADAR-ECG). Three lines labeled in the figure show the mean value and summation of mean value with standard deviation multiply by two. The $(Mean + 2SD)$ of the differences is $5.2\,beats/min$, and $(Mean - 2SD)$ is $-4.6\,beats/min$. The RADAR heartbeat rate results in Fig. 15 are detected by applying Method 3 and DSP 3. The Agreement between RADAR and ECG for the whole of the methods and DSPs are illustrated in Appendix 1 in Figs. A1.1, A1.2, A1.3.

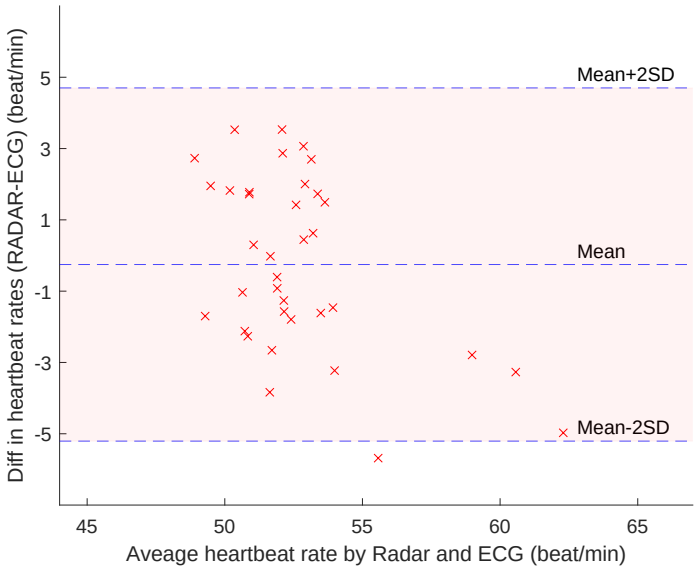

Figure 15. The agreement between two methods of heartbeat rate detecting for Dataset 1 and Dataset 3, using Bland and Altman method [29]. The RADAR heartbeat rate is detected by applying Method 3 and DSP 3.

6 DISCUSSION

6.1 Current study

The vital sign detection was tested with a RADAR sensor, and the algorithm has reasonable accuracy for measuring the respiration, heartbeat rate, and labeling the target as alive or non-alive. It can find the region of interest with the highest micro-vibration related to the human's vital signs. The respiration was identified with the algorithm based on WT. The size of the chest movements for respiration is roughly ten times greater than the heartbeats. Thus, it can affect the heart-related measurement's accuracy in the presence of respiration. Therefore, the system's accuracy for measuring the heartbeat rate is improving when the target holds the breathing.

Different phase extracting methods were used and as it is obvious from Fig. 6, 7, 8, the signals follow the same patterns. In Method 3, a high pass filter was applied through the calculation. Consequently, Method 3 does not have a low-frequency shift, which can be seen in Fig. 7. The phase estimated by Method 1 and 2 is shifting roughly $15mm$ in less than 30 seconds, as in Fig. 7, and the reason is the hand displacement. It is not affecting the accuracy because the corrections were done during each of the DSPs. Phase extracting using Method 1 and Method 2 is based on arctangent demodulation, and there are minor fluctuations in a few numbers of data samples in which the phase data is not unwrapped precisely. Although, the output of arctangent demodulation was more satisfying than unwrapping through the Matlab software. Method 3 has the most stable phase extraction method and is suitable for online data analysis.

The results reveal that by combining Method 3 and DSP 3, the highest accuracy was obtained. This combination has the lowest accuracy variation, with a median accuracy of 96.22%. All of the outliers in Fig. 10 are from Dataset 2, which are captured from the hand movements. The lowest median accuracy was for the combination of Method 1 and DSP 1, and the other combinations have greater accuracy. Method 2 has more than 94% accuracy for all of the possible DSPs, and the results for this method are not affecting by choosing different DSPs. The difference between the methods is not significant, and it not conceivable to specify the actual difference between these methods in the rest position.

The displacement results for Dataset 2 has more significant variations than the other two methods. Recording to Fig. 12 the displacements are approximately two times larger than Dataset 1 and Dataset 3, which means the data is more contaminated with the hand

mechanical vibrations. The Dataset 2 signal is not a reliable source for measuring respiration, but it carries more information in terms of body micro-vibrations and the level of stress. The Dataset 1 and Dataset 3 can show the effect of respiration and is more evident in Fig. 11. After exhaling and pushing out the lung's air, a few apparent peaks related to heart rate can be noticed. It can differ case by case and recording to different body structure and respiration patterns, the shape can have a slight deformation. However, the peaks which are based on the heart rate are more noticeable in lack of respiration.

The transmission scenarios do not significantly affect the accuracy, and the system can measure the vital sign over the clothes and a thin layer of glass. Although recording to Fig. 14, the error bar is more extended when the glass was added. It means the measurements over the thin layer of glass has less accuracy repeatability. The system's accuracy for different transmission scenarios varies from 95.9% to 96.5%, which is a tiny difference, and the other errors such as systematic error or respiration style can affect the results more robust. Dataset 3 has 93.1% accuracy, and although it has less accuracy than Dataset 1, the results are consistent. It is viable to mount the device on the chest and capture the micro-vibrations, but the mechanical vibrations can also affect the signal's quality. Dataset 2 shows less accuracy, which is 91.6% with a deviation of 16.8%, which is a considerable number. It means the in hand setup does not have enough accuracy with the proposed algorithms. The in-hand device can capture extra data regarding mechanical vibrations, and it has to be removed from the signal.

The agreement between the clinical ECG setup and RADAR based system was demonstrated for Dataset 1 and Dataset 3 in Fig. 15. The upper and lower blue horizontal lines emphasize that if the differences have a Gaussian pattern, 95% of the differences are lying between these two lines [29]. The high and low horizontal dash lines of $5.2\,beats/min$, and $-4.6\,beats/min$ means the RADAR heartbeat rate detector may be roughly $5\,beats/min$ above or $5\,beats/min$ below the clinical ECG system. A clinical device and a commercial product do not have the same requirements, and it depends on the target application and the specific requirements.

6.2 Future work

The phase estimation methods can be extended to capture the presence of multiple targets and mark those as alive or non-alive. In this scenario, the vital signs can be captured simultaneously, and method 1, based on peak detection, can be utilized. By applying this idea, it would be possible to extract the vital sign of multiple targets in different ranges.

This study can be continued by using a sensor with multiple receiver channels. In this case, there is a chance to have an angular resolution, and by beamforming, there would be a potential to track two people with the same distance to the RADAR sensor. The other solution is using a MIMO setup and scan the RADAR field of view to add the angular resolution. Also, an optimized radome can be designed for the actual devices depending on the end applications.

7 CONCLUSION

The ability of the RADAR vital sign detection was studied and implemented by $60GHz$ pulsed coherent RADAR system. The algorithm can measure the respiration chest movements with excellent accuracy over various materials. The heartbeat rate was calculated and compared with the clinical reference device. It is possible to calculate the heartbeat rate with fair correctness in case of rest heart rates. Thus, it is a reliable method for sleep monitoring and tracing the apnea. The RADAR is detecting the respiration and the heartbeat rate over a thick layer of clothes. The heartbeat rate is detectable using the RADAR system for estimation of the hand mechanical vibrations. The $60GHz$ RADAR sensors have the potential to be integrated into wearable silicon device solutions.

REFERENCES

[1] B.R. Mahafza. *Radar Systems Analysis and Design Using MATLAB Third Edition*. Taylor & Francis, 2013.

[2] XC112 connector board and XR112 reference board with one A1 radar sensor. Available: https://www.acconeer.com/products, Accessed: Sept.20, 2020.

[3] BCM2711 Raspberry Pi 4 Model B 2GB - ARM® Cortex®-A72 MPU Embedded Evaluation Board. Available: https://www.raspberrypi.org/products/raspberry-pi-4-model-b/specifications/, Accessed: Sept.20, 2020.

[4] A. Santra, I. Nasr, and J. Kim. Reinventing radar: The power of 4d sensing. *Microwave Journal*, 61(12):22–37, 2018.

[5] X. Chen, W. Rhee, and Z. Wang. Low power sensor design for iot and mobile healthcare applications. *China Communications*, 12:42–54, 05 2015.

[6] E. Yavari, H. Jou, V. Lubecke, and O. Boric-Lubecke. Doppler radar sensor for occupancy monitoring. In *2013 IEEE Topical Conference on Power Amplifiers for Wireless and Radio Applications*, pages 145–147, Texas, USA, January, 2013.

[7] F. Lurz, S. Mann, S. Linz, S. Lindner, F. Barbon, R. Weigel, and A. Koelpin. A low power 24 ghz radar system for occupancy monitoring. In *2015 IEEE Radio and Wireless Symposium (RWS)*, pages 111–113, 2015.

[8] Z. Baird, I. Gunasekara, M. Bolic, and S. Rajan. Principal component analysis-based occupancy detection with ultra wideband radar. In *2017 IEEE 60th International Midwest Symposium on Circuits and Systems (MWSCAS)*, pages 1573–1576, 2017.

[9] A. Santra, R. V. Ulaganathan, and T. Finke. Short-range millimetric-wave radar system for occupancy sensing application. *IEEE Sensors Letters*, 2(3):1–4, 2018.

[10] A. Santra, R. V. Ulaganathan, T. Finke, A. Baheti, D. Noppeney, J. R. Wolfgang, and S. Trotta. Short-range multi-mode continuous-wave radar for vital sign measurement and imaging. In *2018 IEEE Radar Conference (RadarConf18)*, pages 0946–0950, Oklahoma City, USA, June, 2018.

[11] M. Zakrzewski, A. Kolinummi, and J. Vanhala. Contactless and unobtrusive measurement of heart rate in home environment. In *2006 International Conference of the IEEE Engineering in Medicine and Biology Society*, pages 2060–2063, New York, USA, August, 2006.

[12] M. Alizadeh, G. Shaker, and S. Safavi-Naeini. Remote heart rate sensing with mm-wave radar. In *2018 18th International Symposium on Antenna Technology and Applied Electromagnetics (ANTEM)*, pages 1–2, Waterloo, Canada, August, 2018.

[13] W. Hu, Z. Zhao, Y. Wang, H. Zhang, and F. Lin. Noncontact accurate measurement of cardiopulmonary activity using a compact quadrature doppler radar sensor. *IEEE Transactions on Biomedical Engineering*, 61(3):725–735, 2013.

[14] M. Zakrzewski and J. Vanhala. Separating respiration artifact in microwave doppler radar heart monitoring by independent component analysis. In *SENSORS, 2010 IEEE*, pages 1368–1371, 2010.

[15] M.A. Richards, W.A. Holm, and J. Scheer. *Principles of Modern Radar: Basic Principles, Volume 1*. Electromagnetics and Radar. Institution of Engineering and Technology, 2010.

[16] D. Montgomery and G. Holmén. Surface classification with millimeter-wave radar for constant velocity devices using temporal features and machine learning. Master's thesis, Lund University, Sweden, 2019.

[17] E. Dagasan. Hand gesture classification using millimeter wave pulsed radar. Master's thesis, Lund University, Sweden, 2020.

[18] M.A. Richards. *Fundamentals of Radar Signal Processing, Second Edition*. McGraw-Hill Education, 2014.

[19] Acconeer python exploration tools, sleep breathing process. Available: https://acconeer-python-exploration.readthedocs.io/en/latest/index.html, Accessed: Sept.20, 2020.

[20] The MathWorks Inc. Available: https://se.mathworks.com/help/matlab/ref/unwrap.html, Accessed: Sept.20, 2020.

[21] J. Wang, X. Wang, L. Chen, J. Huangfu, C. Li, and L. Ran. Noncontact distance and amplitude-independent vibration measurement based on an extended dacm algorithm. *IEEE Transactions on Instrumentation and Measurement*, 63(1):145–153, 2013.

[22] D.L. Gorgas and J.L. McGrath. Vital signs and patient monitoring techniques. *Clinical Procedures in Emergency Medicine: 4th ed.,(JR Roberts and JR Hedges, Eds.), Philadelphia,: Saunders*, pages 3–28, 2004.

[23] M. Zakrzewski. *Methods for Doppler Radar Monitoring of Physiological Signals*. PhD thesis, Tampere University of Technology, Finland, 2015.

[24] N.E. Huang and S.S.P. Shen. *Hilbert–Huang Transform and Its Applications*. World Scientific, 2nd edition, 2014.

[25] L. Debnath and F.A. Shah. *Lecture Notes on Wavelet Transforms*. Compact Textbooks in Mathematics. Springer International Publishing, 2017.

[26] D.J. Kozakoff. *Analysis of radome-enclosed antennas*. Artech House, 2010.

[27] Bittium faros 180 sensor, Advanced system for offline and online ECG. Available: https://www.bittium.com/medical/bittium-faros, Accessed: Sept.20, 2020.

[28] The MathWorks Inc. Available: https://se.mathworks.com/help/stats/boxplot.html, Accessed: Sept.20, 2020.

[29] J.M. Bland and D.G. Altman. Statistical methods for assessing agreement between two methods of clinical measurement. *International Journal of Nursing Studies*, 47(8):931 – 936, 2010.

Appendix 1. Results from the first experiment.

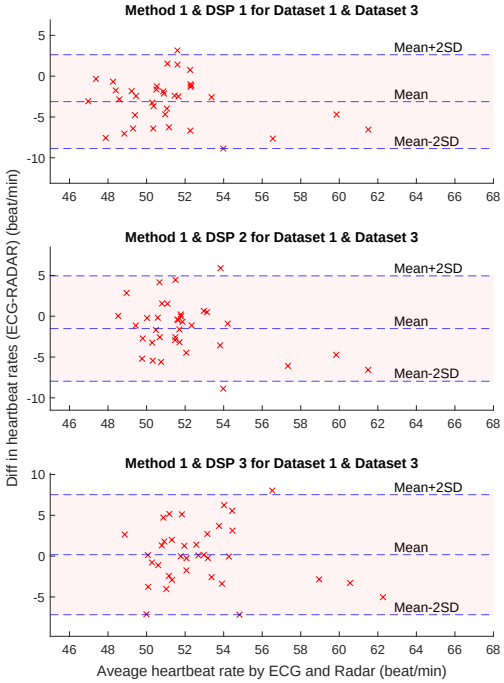

Figure A1.1. The agreement between two methods of heartbeat rate detecting for Dataset 1 and Dataset 3.The RADAR heartbeat rate is detected by applying Method 1 and different DSPs.

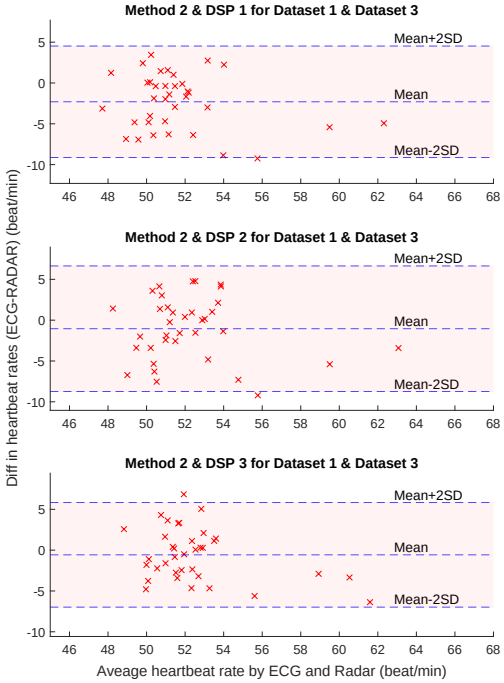

Figure A1.2. The agreement between two methods of heartbeat rate detecting for Dataset 1 and Dataset 3.The RADAR heartbeat rate is detected by applying Method 2 and different DSPs.

(continues)

Appendix 1. (continued)

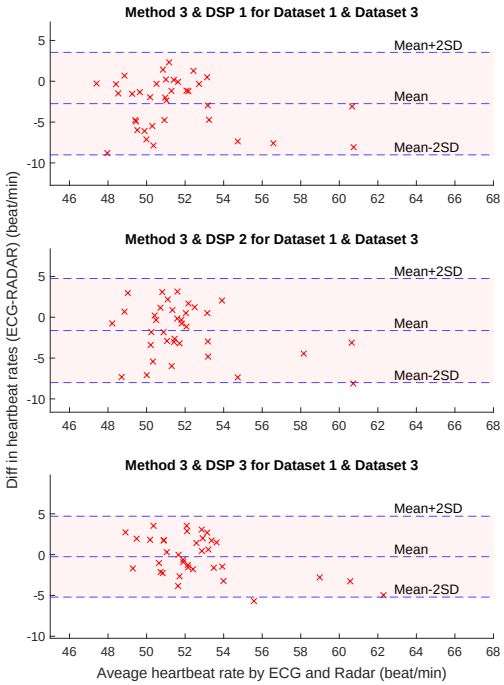

Figure A1.3. The agreement between two methods of heartbeat rate detecting for Dataset 1 and Dataset 3. The RADAR heartbeat rate is detected by applying Method 3 and different DSPs.

(continues)